Check for updates

Interfacially-localized high-concentration electrolytes for high-performance rechargeable aqueous lithium-ion batteries†

Guohong Shen,[a] Shinji Kondou, [b] Gakuto Wada,[a] Hiroki Nakagaki,[a] Masayoshi Watanabe, [c] Kaoru Dokko [a,c] and Kazuhide Ueno ⋆[a,c]

Highly concentrated electrolytes have attracted significant attention because of their ability to enhance electrochemical stability and facilitate the formation of solid electrolyte interphases (SEIs). In particular, the electrolyte materials used in aqueous Li-ion batteries can benefit greatly from these high-concentration effects owing to the poor electrochemical stability of water. Therefore, highly concentrated aqueous electrolytes have recently been employed to achieve wider electrochemical stability windows. However, such high concentrations lead to increased electrolyte viscosity, reduced ionic conductivity, higher costs, and decreased energy density. In addition, employing diluents to create localized high-concentration electrolytes in aqueous systems is challenging, unlike in non-aqueous systems. In this study, we developed novel "interfacially-localized high-concentration electrolytes" using a fluorinated anionic surfactant, lithium nonafluoro-1-butanesulfonate (LiNFBS) (2.13 M), in conjunction with a divalent salt, magnesium(II) bis(trifluoromethanesulfonyl)imide (Mg(TFSI)$_2$) (0.74 M). Using this electrolyte, we achieved a wide electrochemical stability window (ESW) of 3.3 V, a high Li$^+$ transference number, elevated ionic conductivity (34.0 mS cm^{-1}), low viscosity (19.2 mPa s), excellent interfacial wettability, and superior SEI formation. Based on the remarkable performance of this electrolyte, lithium titanium phosphate (LTP)/lithium manganate (LMO) full cells demonstrated high-rate capability at 40 C and were maintained for over 750 stable cycles at a current density of 5 C. Thus, this design concept may provide new avenues for the development of next-generation high-performance aqueous electrolytes.

Broader context

Aqueous electrolytes have been regarded as among the most exciting next-generation energy storage systems owing to their high ionic conductivity and potentially low cost, while the narrow electrochemical stability window (ESW) has always been the main challenge for this technology. Recently, "water-in-salt" and "hydrate-melt" have emerged as effective strategies to widen the ESW. Nevertheless, the high cost, low ionic conductivity, and high viscosity greatly impede their widespread application. In this work, we proposed a novel concept of aqueous electrolytes based on the anionic surfactant of Li salt and divalent salt additives. This concept was demonstrated for the first time, showing that fluorinated hydrophobic anions of the surfactant endow the aqueous electrolytes with a significantly enhanced ESW, superior transport properties, a higher Li$^+$ transference number and excellent battery performance of aqueous Li-ion batteries *via* the self-assembly of the surfactant in the bulk and at the interface. The new concept of interfacially-localized high-concentration electrolytes allows for not only higher ionic conductivity (34.0 mS cm^{-1}), lower viscosity (19.2 mPa s), and a high Li$^+$ transference number in the bulk solution but also effective solid–electrolyte interphase (SEI) formation at the interface, leading to the widening of the ESW and better electrochemical performance in aqueous LiTi$_2$(PO$_4$)$_3$/LiMn$_2$O$_4$ full cells.

[a]Department of Chemistry and Life Science, Yokohama National University, 79-5 Tokiwadai, Hodogaya-ku, Yokohama 240-8501, Japan. E-mail: ueno-kazuhide-rc@ynu.ac.jp

[b]Department of Materials Engineering Science, Graduate School of Engineering Science, Osaka University, 1-3 Machikaneyama, Toyonaka, Osaka 560-8531, Japan

[c]Institute of Advanced Sciences, Yokohama National University, 79-5 Tokiwadai, Hodogaya-ku, Yokohama 240-8501, Japan

†Electronic supplementary information (ESI) available. See DOI: https://doi.org/10.1039/d4eb00036f

Introduction

Owing to increased environmental pollution, there is a growing demand for the widespread adoption of green solvents in the industry.[1] Electrolytes, comprising a solvent and salt, function as a medium for ion transport in electrochemical energy storage systems. However, many of these systems rely on non-aqueous solvents.[2,3] Aqueous electrolytes, which utilize water as a super-green solvent owing to their nontoxicity, low cost, and environmental benignity, have garnered significant interest as potential candidates for next-generation batteries. Despite these advantages, including high ionic conductivity, the narrow electrochemical stability window (ESW) of water (1.23 V) hinders their commercialization. To address this issue, "water-in-salt electrolyte (WiSE)" composed of 21 mol kg^{-1} (~5 M) lithium bis(trifluoromethanesulfonyl)imide (LiTFSI) has been employed to extend the ESW of water to 3.0 V. Furthermore, hydrate melt electrolytes with a concentration of 27.8 mol kg^{-1} further widen the ESW.[4,5]

Highly concentrated electrolytes (HCEs) can form a suitable solid–electrolyte interphase (SEI) in non-aqueous electrolytes.[6–8] However, the SEI is considered unstable in aqueous media because of its high solubility, while it always kinetically protects the cathode and anode under the stability of non-aqueous electrolytes.[5,9] The WiSE containing 21 mol kg^{-1} LiTFSI was found to form a dense and relatively stable SEI containing LiF in aqueous media through a unique solvation sheath and the decomposition of the TFSI$^-$ anion.[5] Our previous research demonstrated that adding divalent salts, such as Mg(TFSI)$_2$ to WiSE can form less-soluble MgF$_2$ as the SEI component, effectively suppressing water decomposition and further expanding the ESW.[10,11] However, such ultrahigh concentrations have disadvantages such as low ionic conductivity, high viscosity, high density, and high cost. Therefore, new strategies are required to overcome these limitations.

The concept of "localized high-concentration electrolytes (LHCEs)" first emerged from studies that utilized non-disrupting hydrofluoroethers (HFE) as diluents for non-aqueous ether-based HCEs.[12,13] Subsequent research explored the application of LHCEs in Li-metal batteries.[14,15] Using a low-polarity diluent enhances conductivity by reducing its viscosity while simultaneously preserving the local ion coordination structure because of the lack of coordination with cations and anions. This allows for the advantages of HCEs while retaining the characteristics of a dilute electrolyte.[12,13] However, this approach using a low-polarity diluent to yield LCHEs cannot be applied to aqueous electrolytes because low-polarity diluents are usually immiscible with aqueous electrolytes.

Surfactants, which possess hydrophilic heads and hydrophobic tails, exhibit unique properties both in bulk solution and at interfaces.[16] Ionic surfactants can form micelles in bulk solutions and adsorb at the interface. Notably, the surface orientation/aggregation of surfactants can reduce interfacial water owing to the hydrophobicity of the tail groups.[17,18] Meanwhile, by utilizing anionic surfactants as sources of Li$^+$, diffusion and migration of the anionic species can be signifi-cantly restricted *via* micelle formation in the bulk. This, in turn, leads to a high Li$^+$ transference number. Although surface-accumulated surfactants act as protective layers against water electrolysis at the electrode, they do not completely suppress water decomposition.[19]

In this study, we propose the concept of "interfacially-localized high-concentration electrolytes (ILHCEs)" for aqueous electrolytes, composed of a fluorinated anionic surfactant, lithium nonafluoro-1-butanesulfonate (LiNFBS) and a divalent salt additive, magnesium(II) bis(trifluoromethanesulfonyl)imide (Mg(TFSI)$_2$). The surface-active properties of LiNFBS in aqueous electrolytes in the absence and presence of Mg(TFSI)$_2$ were studied using surface tension and contact angle measurements. The concentration-dependent ion transport properties, including ionic conductivity, self-diffusion coefficients of ions, and viscosity, were thoroughly elucidated to demonstrate the high Li-ion transport properties of ILHCEs. The enhanced ESW was confirmed by electrochemical measurements and rationalized by surface analyses of robust SEI formation with divalent cations. The rate performance and cycling stability of lithium manganate (LMO)/lithium titanium phosphate (LTP) full cells were elucidated to leverage the unique transport and interfacial properties of ILHCEs.

Experimental section

Materials

Lithium nonafluoro-1-butanesulfonate (LiNFBS) and magnesium(II) bis(trifluoromethanesulfonyl)imide (Mg(TFSI)$_2$) were purchased from Tokyo Chemical Industry. Lithium nitrate (LiNO$_3$), lithium bis(trifluoromethanesulfonyl)imide (LiTFSI), lithium trifluoromethanesulfonate (LiOTf), lithium sulfate (Li$_2$SO$_4$), lithium acetate dihydrate, phosphoric acid, tannic acid, trifluoroacetic acid, and *N*-methyl-2-pyrrolidone (NMP) were purchased from Wako Pure Chemicals. Polyvinylidene fluoride (PVDF) was purchased from Kishida Chemical Co. Ltd. Tetrabutyl titanate and lithium manganese oxide (LMO) were purchased from Sigma-Aldrich. Ultrapure water (~18 MΩ cm) was obtained by using a Milli-Q Integral 3 Pure water machine. Each salt was dissolved in ultrapure water in an appropriate ratio to prepare the electrolyte.

Synthesis of carbon-coated LiTi$_2$(PO$_4$)$_3$

The synthesis of carbon-coated LiTi$_2$(PO$_4$)$_3$ (LTP) was performed through a sol–gel method followed by high-temperature calcination, based on established procedures.[20] First, tetrabutyl titanate (3.412 g) and lithium acetate dihydrate (0.525 g) were dissolved in 50 mL of absolute ethanol. Phosphoric acid (1.754 g) and tannic acid (0.578 g) were dissolved in 20 mL of absolute ethanol in a separate container. This mixture was gradually combined with the mixture of tetrabutyl titanate and lithium acetate solution, and the resultant solution was stirred continuously for 3 h at 50 °C. The temperature was then increased to 70 °C to ensure complete evaporation of the solvent. The resulting mixture was ground in a

mortar to produce a dark brown precursor. This precursor was placed in a graphite boat and subjected to calcination in a tube furnace under an argon atmosphere, with the calcination conditions set at 750 °C for 5 h and a heating rate of 5 °C min^{-1}. The successful synthesis of LTP was confirmed by X-ray diffraction (XRD) patterns (Fig. S1†).

Material characterization

Ionic conductivity (σ) was determined using an impedance analyzer (VMP-3, Biologic Science Instruments) across a frequency range of 500 kHz to 100 mHz, with a voltage amplitude of 10 mV. Before the measurement, a platinized platinum electrode cell (CG-511B, DKK-TOA) was calibrated using a 0.01 M KCl aqueous solution. Viscosity and density were assessed using SVM3000 (Anton Paar). Morphological analyses were performed using a scanning electron microscope (Hitachi FE-SEM SU8000, Japan).

The self-diffusion coefficients of H_2O, Li ions, and NFBS anions were determined through pulsed-field gradient nuclear magnetic resonance (PFG-NMR) measurements using a JEOL-ECX 400 spectrometer. Measurements were performed using a stimulated echo (STE) pulse sequence with sinusoidal PFG.[21]

The oxidative and reductive stabilities of the electrolytes were examined via linear sweep voltammetry (LSV) using a VMP-3 electrochemical workstation (Biologic Science Instruments). LSV measurements were performed at a scan rate of 1 mV s^{-1} in a three-electrode setup, incorporating glassy carbon (GC) or aluminum (Al) as the working electrodes, a platinum wire as the counter electrode, and an Ag/AgCl reference electrode in saturated aqueous KCl solution. Electrochemical impedance spectroscopy (EIS) was performed on the Al current collector using a VMP-3 electrochemical workstation (Biologic Science Instruments) with an AC voltage of 10 mV in the frequency range of 10 mHz–500 kHz before and after potentiostatic polarization for 2 hours at −1.2 V vs. Ag/AgCl to study the formation of a SEI in the studied electrolytes.

X-ray diffraction (XRD) patterns of the prepared LTP were obtained using a Rigaku Ultima IV X-ray diffractometer equipped with Cu Kα (λ = 0.154 nm) radiation (Fig. S1†). Thermogravimetric analysis (TGA) was conducted using a STA7200 Thermogravimetry/Differential Thermal Analyzer (Hitachi High-Tech Science Corporation).

The cathode was prepared by mixing commercial $LiMn_2O_4$ (LMO), acetylene black (AB), and PVDF in NMP at a weight ratio of 80 : 10 : 10 using a mixing machine. The anode was composed of as-prepared $LiTi_2(PO_4)_3$ (LTP), AB, and PVDF in NMP at a weight ratio of 70 : 20 : 10, and they were mixed using a machine. The resulting slurry was coated onto titanium foil and carbon-coated aluminum current collectors with diameters of 15.95 and 13.82 mm, respectively. The electrodes were dried at 80 °C under vacuum for 12 h. The loading amount of LTP was approximately 2–3 mg cm^{-2}, and the loading ratio of LTP to LMO was approximately 1.3–1.5. The specific capacities were calculated based on the weight of the anode active material (LTP). Before use, the cathode and anode sheets were pressed using a hydraulic press (10 MPa) to ensure that the active materials adhered well. To reduce unwanted side reactions between the electrolyte and the components of the coin cell, an 18 mm diameter Ti foil was positioned between the positive electrode sheet and the bottom of the positive casing. Additionally, an 18 mm diameter aluminum foil was placed between the negative electrode sheet and the spacer, which was wrapped in aluminum foil.[4]

Glass filter paper (GA-55, Advantec) was used as the separator. CR2032-type coin cells were assembled for electrochemical testing under a controlled atmosphere. Galvanostatic discharge/charge measurements were conducted within a voltage window of 0.4–1.8 V. All electrochemical measurements were performed at a stable temperature of 30 °C.

The contact angles were measured using a smart contact mobile device (A511). An automatic surface tension meter (CBVP-Z) was used to measure the surface tension. Attenuated total reflection (ATR)–Fourier transform infrared (FTIR) spectra were acquired using a JASCO FT/IR-6600 spectrometer fitted with a PIKE Technologies horizontal ATR accessory containing a ZnSe crystal. The spectra were recorded over 128 scans within a wavenumber range of 1000–4600 cm^{-1}, achieving an optical resolution of 4.0 cm^{-1}. X-ray photoelectron spectroscopy (XPS) was performed using a PHI Quantera SXM ULVACPHI spectrometer. After performing chronoamperometry (−1.2 V vs. Ag/AgCl for 20 h in various electrolytes), the Al electrode was rinsed with 1,2-dimethoxyethane (DME, Kishida Chemical Co.) to remove any residual electrolyte, then dried under vacuum for 24 h. The XPS binding energy calibration was achieved using the C 1s peak for adventitious carbon at 284.8 eV.

Results and discussion

Fig. 1 shows the chemical structures of the anionic surfactant Li salt LiNFBS and the less surface-active Li salts $LiNO_3$, LiTFSI, and lithium trifluoromethane sulfonate (LiOTf). Based on our earlier findings, $Mg(TFSI)_2$ was added to the aqueous electrolytes in an effort to create a hardly soluble SEI.[10,11] An aqueous electrolyte of 1 M Li_2SO_4 was used as a reference electrolyte in this study. The composition of the electrolyte samples studied is represented as the mixed molar ratio of the salts and water, that is, LiNFBS-$x$$H_2O$ without the $Mg(TFSI)_2$ additive and LiNFBS-$y$$Mg(TFSI)_2$-$x$$H_2O$ with the divalent salt additive, where x and y are the mixed molar ratios of H_2O and $Mg(TFSI)_2$ with respect to LiNFBS, respectively. The corresponding molar concentrations of each sample are listed in Table S1 (without $Mg(TFSI)_2$) and S2† (with $Mg(TFSI)_2$). As shown in Fig. S2,† gel-like substances (red dashed circle) were phase-separated and precipitated from a concentrated LiNFBS-11H_2O solution. In contrast, LiNFBS-12H_2O did not form gel-like substances and remained transparent and homogeneous. Therefore, the molar ratio of LiNFBS/H_2O at 1 : 12 was selected as the maximum concentration of LiNFBS in the
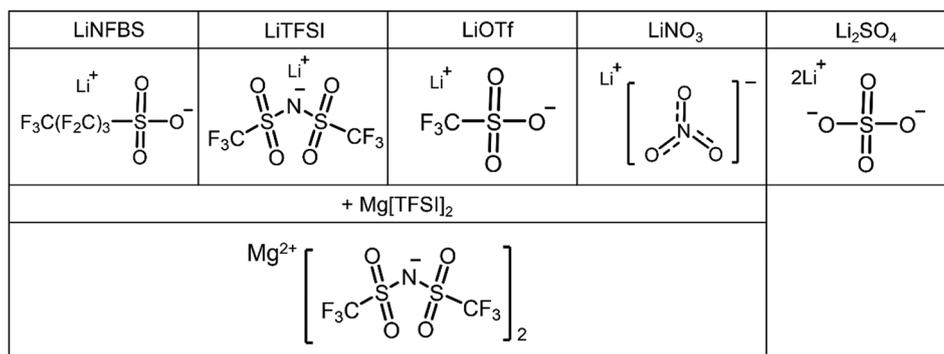
Fig. 1 The chemical structures of the surfactant and the salt used in this study.

aqueous electrolyte studied in this work. Compared to traditional hydrocarbon-based anionic surfactants, fluorinated surfactants such as LiNFBS provide surfactant activity even with a shorter chain length of the hydrophobic tail.[22] The strong electron-withdrawing effect (or weaker Lewis basicity) of perfluorinated sulfonates is expected to impart higher electrochemical oxidative stability unlike strongly Lewis basic anions such as NO_3^-, and SO_4^{2-}.[23]

Micelles are nanoscale aggregates formed by the self-assembly of surfactant molecules. As shown in Fig. 2(a), micelles are formed when the surfactant concentration exceeds the critical micelle concentration (CMC).[24] The formation of micellar structures was elucidated by measuring the CMC of the surfactant solutions.[25,26] To determine the CMC, the surface tension of the samples was measured at different salt concentrations. The surface tension of the LiNFBS solution without the Mg(TFSI)$_2$ additive is shown as a function of the molar concentration of the salt in Fig. 2(b). With increasing LiNFBS concentration, the surface tension gradually decreased until it stabilized at a relatively constant level. The concentration at which the surface tension levels off was assigned as the CMC.[27] The CMC of LiNFBS was found to be approximately 0.65 M, which is higher than that of the previously studied lithium dodecyl sulfate (LDS, 0.07 M).[19] This suggests that $NFBS^-$ exhibits lower hydrophobicity compared to dodecyl sulfate, requiring a higher concentration to form stable micellar aggregates in water.[26] We also measured the surface tension of the LiNFBS solutions in the presence of Mg(TFSI)$_2$ (Fig. 2(c)). In a preliminary test, Mg(TFSI)$_2$ was found to exhibit weak surfactant activity even without LiNFBS: the surface tension was reduced from 72 mN m^{-1} in pure water to 45.3 mN m^{-1} in 0.74 M Mg(TFSI)$_2$ solution (Table S3†). Therefore, we cannot accurately determine the CMC of LiNFBS in a 0.74 M Mg(TFSI)$_2$ solution: the obtained value represents a mixed CMC of both components. As shown in Fig. 2(c), the surface tension further decreased at a LiNFBS concentration of 0.90 M, suggesting the formation of mixed micellar aggregates.

Attenuated total reflectance Fourier transform infrared (ATR FTIR) spectroscopy was performed to investigate changes in the hydrogen bond network of water in LiNFBS solutions. As shown in Fig. 2(d), compared to pure water, the OH stretch-

ing mode of the concentrated surfactant solution (LiNFBS-12H$_2$O, 2.7 M) shifts to a higher wavenumber of ~3432 cm^{-1}. This is indicative of enhanced hydration around the charged head groups of the surfactants and the disruption of the orderly hydrogen bonding network of pure water by the formation of micellar structures.[28,29] The addition of Mg(TFSI)$_2$ further causes the OH stretching band to shift to approximately 3496 cm^{-1}. The addition of structure breaking Mg^{2+} significantly disrupted the ordered hydrogen bonding network *via* strong hydration of Mg^{2+}.[30] Likewise, as shown in Fig. S3(a) and (b),† the OH stretching band shifted to higher wavenumber upon increasing either the LiNFBS concentration or the Mg(TFSI)$_2$ concentration. These results further support that both LiNFBS and Mg(TFSI)$_2$ can disrupt the hydrogen bond network of water through their hydration with water molecules (Fig. 2(e)).

Fig. 2(f) and (g) display the contact angles on the aluminum (Al) substrate for the 1 M Li$_2$SO$_4$ reference electrolyte and 2.7 M LiNFBS solution (corresponding to LiNFBS-12H$_2$O). Compared with the 1 M Li$_2$SO$_4$ reference electrolyte (95.57°), the surfactant solutions of 2.7 M LiNFBS exhibited a significantly lower contact angle (14.81°). The adsorption and ordered arrangement of LiNFBS at the interface reduces the total free energy of the droplets on the solid surface, thereby affording good wettability of the LiNFBS-based surfactant solutions on the substrate.[31] The later section discusses how the enhanced wettability of electrolytes containing LiNFBS significantly impacts the mass transfer of Li-ions in the porous composite electrodes of high-performance aqueous lithium-ion batteries.

To elucidate the bulk ion transport properties, the self-diffusion coefficients of Li-ion (D_{Li^+}), anion (D_-) and water (D_{H_2O}) were determined using PFG-NMR. The diffusivity data were plotted against the mixed ratio of the Li salt to water, LiNFBS-xH$_2$O. As shown in Fig. 3(a), in LiNFBS solutions without Mg(TFSI)$_2$, all the D_{Li^+}, D_-, and D_{H_2O} values gradually decreased with decreasing molar ratio of water to LiNFBS. Notably, D_- was significantly lower than D_{Li^+} and D_{H_2O} in all the concentration ranges studied. This suggests that the formation of micellar aggregates of $NFBS^-$ anions significantly hindered their mobility. The more restricted diffusion of the
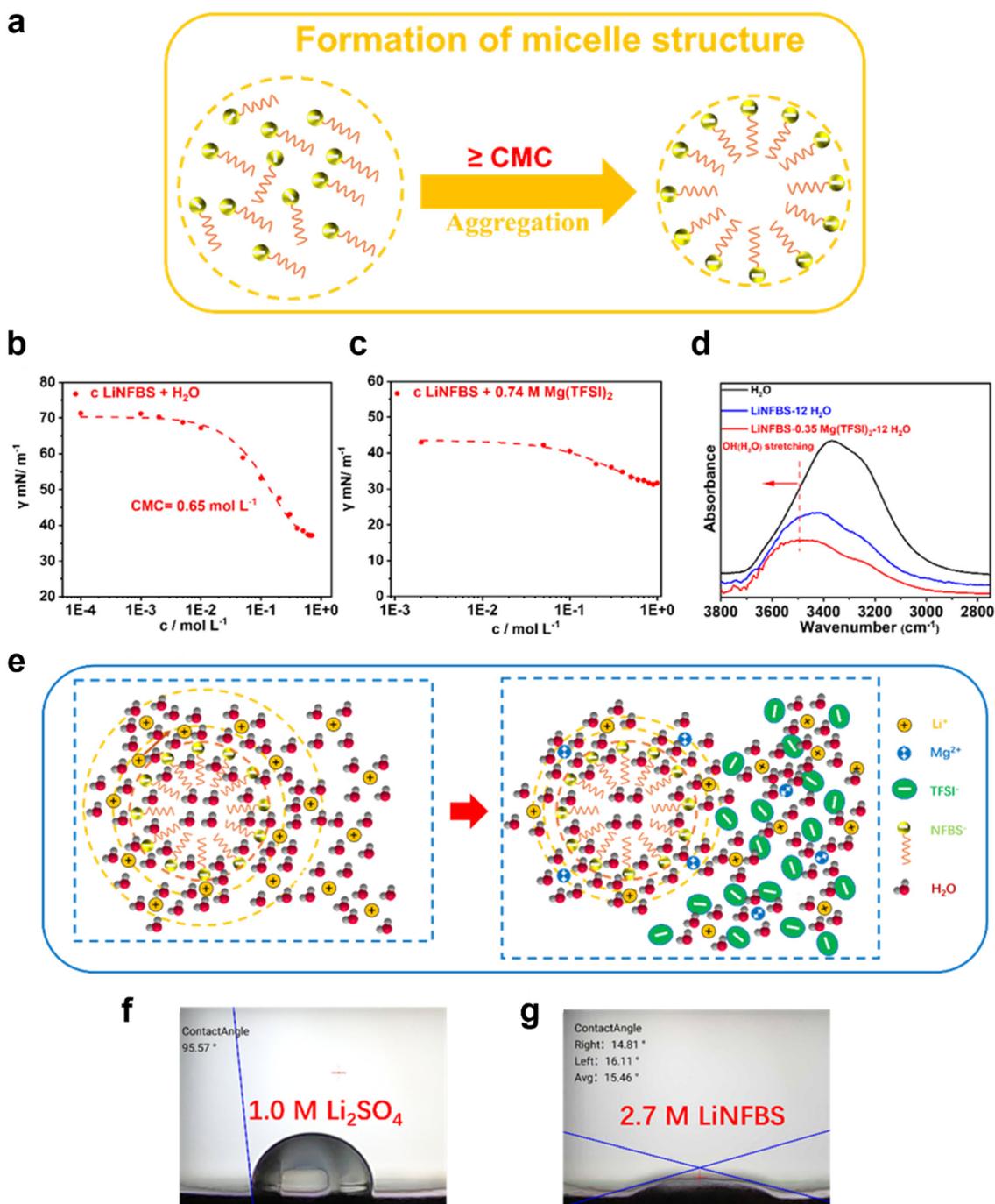
Fig. 2 (a) Schematic illustration of micelle formation, and surface tension of (b) the LiNFBS solutions and (c) the LiNFBS solutions containing 0.74 M Mg(TFSI)$_2$ with different concentrations of LiNFBS, (d) FTIR spectra of H$_2$O, LiNFBS-12H$_2$O, and LiNFBS-0.35Mg(TFSI)$_2$-12H$_2$O, and (e) speculated hydration structures in the micellar structure before and after the addition of Mg(TFSI)$_2$, and contact angles of (f) 1 M Li$_2$SO$_4$ and (g) 2.7 M LiNFBS (LiNFBS-12H$_2$O) solutions on the Al substrate.

NFBS$^-$ aggregates leads to a more selective diffusion of Li$^+$ ions as they are not bound or restricted by the large anion clusters. Fig. 3(b) shows the self-diffusion coefficients in LiNFBS-12H$_2$O with different Mg(TFSI)$_2$ concentrations. Although all diffusion coefficients decreased with increasing Mg(TFSI)$_2$ content, the reduction in D_{H_2O} was the most promi-

nent among those of the ions and solvents. The strong hydration of Mg^{2+} was responsible for the significant decrease in D_{H_2O}. With the addition of Mg(TFSI)$_2$, D_- of NFBS anions remained notably low compared to D_{Li^+}, D_{H_2O} and D_- of TFSI anions for LiNFBS-yMg(TFSI)$_2$-12H$_2$O. These findings imply that the micellar structures of NFBS anions were not substan-

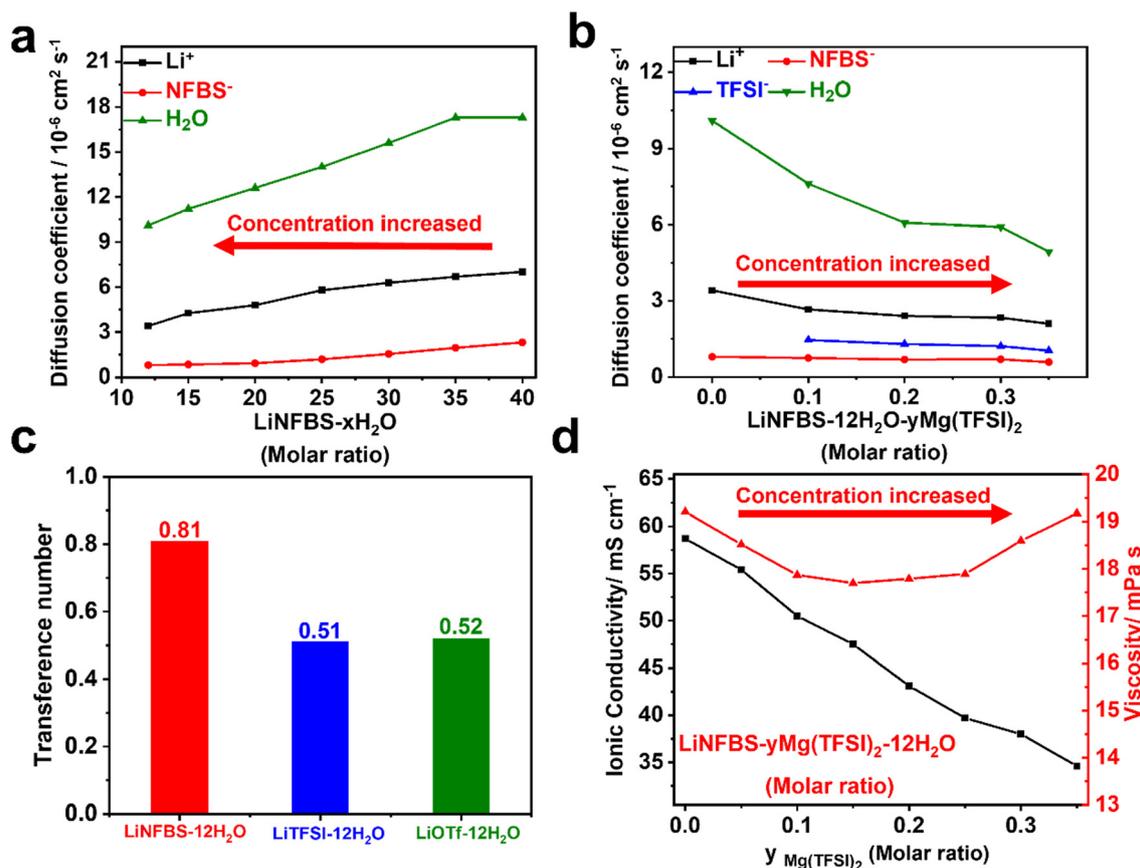**Fig. 3** Transport properties: self-diffusion coefficient of Li ions, anions, and H$_2$O in (a) LiNFBS-xH$_2$O and (b) LiNFBS-yMg(TFSI)$_2$-12H$_2$O, (c) apparent Li$^+$ transference number, $t_{Li^+}^{NMR}$, of LiNFBS-12H$_2$O, LiTFSI-12H$_2$O, and LiOTf-12H$_2$O, and (d) the ionic conductivity and viscosity of LiNFBS-yMg (TFSI)$_2$-12H$_2$O.

tially disturbed by the addition of Mg(TFSI)$_2$. These diffusivity data strongly support the formation of micellar aggregates of NFBS$^-$ and the significant hydration of Mg^{2+} found in the surface tension measurements and FTIR spectra (Fig. 2 and S3†).

The apparent value of the Li-ion transference number ($t_{Li^+}^{NMR}$) in LiNFBS-xH$_2$O can be estimated from the diffusion coefficients of the ions according to the following equation:[32]

$$t_{Li^+}{}^{NMR} = \frac{D_{Li^+}}{D_{Li^+} + D_-}$$

Note that $t_{Li^+}^{NMR}$ is based on the assumption that the ions are fully dissociated and independently mobile without any interaction with other ionic species, as predicted by the Nernst–Einstein relationship for ideal electrolyte solutions. Therefore, the actual Li-ion transference number can be affected by ion–ion interactions and the correlated motions of ions in concentrated electrolyte solutions.[33] Nevertheless, to highlight the efficient Li-ion transport in anionic surfactant-based electrolytes, we compared $t_{Li^+}^{NMR}$ values of LiNFBS solutions with those of solutions using other Li salts, such as LiTFSI and LiOTf. Another reason for using $t_{Li^+}^{NMR}$ is that the typical Li-ion transference number measurements using a sym-

metric cell of Li metal electrodes are not applicable in aqueous systems. As shown in Fig. 3(c), LiNFBS-12H$_2$O exhibited a higher $t_{Li^+}^{NMR}$ value (0.81) compared to its counterparts, LiTFSI-12H$_2$O (0.51) and LiOTf-12H$_2$O (0.52). The higher $t_{Li^+}^{NMR}$ value for LiNFBS-12H$_2$O suggests the more restricted anion diffusion in the form of the aggregates of NFBS$^-$, while allowing more selective diffusion of Li ions. Although fluorinated anions, TFSI$^-$ and OTf$^-$, have the potential to form an aggregate in aqueous solutions, the lower $t_{Li^+}^{NMR}$ values close to 0.5 suggest no significant aggregate formation of these anions. For LiNFBS-y Mg(TFSI)$_2$-12H$_2$O solutions, $t_{Li^+}^{NMR}$ could not be estimated since our PFG-NMR facility does not allow for the measurements of the self-diffusion coefficient of Mg^{2+}.[34] As observed in Fig. 2(c) and 3(b), the micelle aggregates of NFBS$^-$ anions still persist with the addition of Mg(TFSI)$_2$. Hence, a high $t_{Li^+}^{NMR}$ value can be expected owing to the much higher D_{Li^+} value than the D_- value of NFBS$^-$ and TFSI$^-$ anions and the lower concentration of Mg(TFSI)$_2$ than LiNFBS.

The ionic conductivities and viscosities were studied for the LiNFBS-xH$_2$O solutions. Table S1† illustrates that in the absence of Mg(TFSI)$_2$, the viscosity progressively rose as the molar ratio of water, x, decreased. The enhanced interactions between Li ions, NFBS$^-$ anions, and water molecules contribu-

ted to the increase in the viscosity at higher LiNFBS concentrations. Furthermore, the viscosity of the solutions above the CMC was affected by the intermicellar repulsive interactions of $NFBS^-$ aggregates. The ionic conductivity initially increased and then decreased with increasing LiNFBS concentration. The initial increase in conductivity was attributed to an increase in the charge carriers, while the subsequent reduction in conductivity was ascribed to the increased viscosity.

For LiNFBS-yMg(TFSI)$_2$-12H$_2$O solutions, the viscosity did not show a simple monotonical change unlike the binary mixtures of LiNFBS-xH$_2$O. The viscosity initially decreased slightly with increasing Mg(TFSI)$_2$, reaching a minimum at a molar ratio of LiNFBS-0.15Mg(TFSI)$_2$-12H$_2$O (Fig. 3(d) and Table S2†). Subsequently, the viscosity was enhanced by a further increase in the concentration of Mg(TFSI)$_2$. In the lower-concentration (y) region, the addition of Mg(TFSI)$_2$ increased the ionic strength of the solution. Therefore, the electrostatic shielding effect derived from the increased Mg^{2+} ion concentration reduces the electrostatic repulsion between the micellar aggregates in LiNFBS-12H$_2$O. This led to an initial decrease in the viscosity of the solution upon the addition of Mg(TFSI)$_2$. However, in the higher concentration range, the excessive addition of Mg(TFSI)$_2$ enhanced the viscosity of the aqueous solution primarily owing to the reduced fraction of uncoordinated water molecules *via* the more pronounced hydration of Mg^{2+}.

The ionic conductivity decreased monotonically with increasing Mg(TFSI)$_2$ and did not increase, despite a reduction in viscosity at lower Mg(TFSI)$_2$ contents. This suggests that the addition of Mg(TFSI)$_2$ reduces the degree of ionic dissociation of the LiNFBS salt in association with an increase in the ionic strength. At higher concentrations, the increase in viscosity, along with a decrease in the degree of ionic dissociation, significantly reduced the overall ionic conductivity of the solution.

As shown in Table 1, although the addition of Mg(TFSI)$_2$ reduced the ionic conductivity of the electrolyte, LiNFBS-0.35Mg(TFSI)$_2$-12H$_2$O exhibited a high ionic conductivity of 34.0 mS cm^{-1}, which is significantly greater than that of WiSE (9.1 mS cm^{-1}), and hydrate-melt (3.0 mS cm^{-1}). Meanwhile, the viscosity of the electrolyte showed no significant change (19.2 mPa s) before and after the addition of Mg(TFSI)$_2$, remaining well below that of WiSE (51.6 mPa s), hydrate-melt (203.0 mPa s), and non-aqueous HCEs.[4,5,35,36] Additionally, LiNFBS-0.35Mg(TFSI)$_2$-12H$_2$O exhibited a lower Li salt concentration and density than the WiSE and hydrate-melt electrolytes. Lower density is also advantageous for

improving the energy density of batteries. Notably, the water content in LiNFBS-0.35Mg(TFSI)$_2$-12H$_2$O increased by 2–3 times compared to the reported WiSE and hydrate melt while still achieving a remarkable ESW, as discussed in the latter part (3.3 V, Fig. 4(a)). In the following section, LiNFBS-0.35Mg(TFSI)$_2$-12H$_2$O is used as an interfacially-localized, highly concentrated electrolyte (ILHCE) in aqueous Li-ion secondary batteries, and its electrochemical properties are investigated.

Fig. 4(a) shows the ESW of LiNFBS-0.35Mg(TFSI)$_2$-12H$_2$O on Al and GC electrodes for reductive and oxidative stability, respectively. The ILHCE showed onset potentials of −1.63 and 1.67 V *vs.* Ag/AgCl for reductive and oxidative decompositions, respectively. As a result, the ESW has been extended to 3.3 V. Fig. 4(a) shows the cyclic voltammograms (CVs) of the LTP and LMO electrodes as the working electrodes, Pt as the counter electrode, and Ag/AgCl as the reference electrode. The operating potentials of LTP as the negative electrode and LMO as the positive electrode fell within the ESW of the LiNFBS-0.35Mg(TFSI)$_2$-12H$_2$O electrolyte, suggesting that the wide ESW allowed the LTP/LMO full batteries to operate effectively. Cyclic voltammetry of the LTP/LMO full cell was also performed in the potential range of 0.4–1.8 V to confirm the applicability of
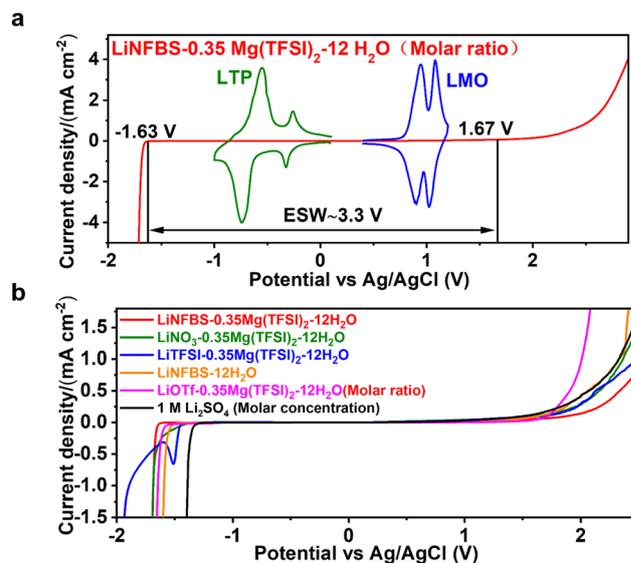

Fig. 4 (a) The electrochemical stability window of LiNFBS-0.35Mg(TFSI)$_2$-12H$_2$O on the Al electrode with cyclic voltammograms of the LTP anode and LMO cathode. (b) Electrochemical stability window (ESW) of LiNFBS-0.35Mg(TFSI)$_2$-12H$_2$O, LiNO$_3$-0.35Mg(TFSI)$_2$-12H$_2$O, LiTFSI-0.35Mg(TFSI)$_2$-12H$_2$O, LiOTf-0.35Mg(TFSI)$_2$-12H$_2$O, LiNFBS-12H$_2$O, and 1 M Li$_2$SO$_4$.

Table 1 Physical properties of studied electrolytes, hydrate-melt electrolytes, and water-in-salt electrolytes at 30 °C

Electrolytes (molar ratio)	η (mPa s)	σ (mS cm^{-1})	Molar concentration c_{Li^+} : $c_{Mg^{2+}}$ (mol L^{-1})	Water content (wt%)	Density ρ (g cm^{-3})
LiNFBS-0.35Mg(TFSI)$_2$-12H$_2$O **(this work)**	**19.2**	**34.0**	**2.13 : 0.74**	**29.4**	**1.54**
0.7LiTFSI : 0.3LiBETI : 2H$_2$O (hydrate melt)[4]	203.0	3.0	3.54 : 1.52	10.2	1.78
LiTFSI : 2.6H$_2$O (water-in-salt)[5]	51.6	9.1	5.15	14.0	1.72

the electrolyte to full cells (Fig. S4†). Although the wide ESW of 3.3 V was not fully utilized in this study, galvanostatic discharge/charge measurements of the full cell were performed over a voltage range of 0.4–1.8 V, consistent with the operating window of the LTP/LMO full cell configuration to demonstrate charge–discharge performance of aqueous Li-ion batteries.

In Fig. 4(b), the effects of Li salt species on the ESWs of aqueous electrolytes containing the same molar ratio of Mg (TFSI)$_2$ and H$_2$O were studied. The traditional 1 M aqueous Li$_2$SO$_4$ electrolyte showed the narrowest ESW among the studied electrolytes. A comparative analysis of the ESW with different Li salts revealed that the use of LiNFBS yielded a wider ESW than the other Li salts, LiNO$_3$ and LiTFSI. Both reductive and oxidative stabilities were enhanced in electrolytes with LiNFBS in the presence of Mg(TFSI)$_2$. Given a little higher Lewis basicity of NFBS$^-$ than TFSI$^-$,[37] the higher oxidative stability of the ILHCE with LiNFBS suggests that the oxidative stability was dominated by a specific interfacial effect rather than the intrinsic oxidative stability of the anions.

In comparison to LiNO$_3$ and LiTFSI, LiNFBS has the surface activity as discussed in Fig. 2(b) and (c), enabling it to adsorb and aggregate at the electrode surface.[38] At the solid–liquid interface, the surfactant molecules arrange themselves into monolayers or multilayers.[38–40] The adsorption and aggregation of the surfactants has a dual effect at the interface. First, surfactants densely adsorbed on the surface can impart hydrophobicity, which expels and reduces interfacial water, leading to the suppression of water decomposition at the electrode interface.[41–43] Second, the surface-adsorbed anionic surfactant layers create a localized high-salt-concentration region extending from the surface to the Helmholtz plane.[17,18] Thus, the interfacially localized and highly concentrated NFBS$^-$ anions

with counter cations of Li$^+$ and Mg^{2+} can significantly benefit the protection of the electrode surface *via* the formation of an effective passivation layer as demonstrated in WiSE and hydrate melt.[4,5] This localized high-salt concentration region at the interface enables robust SEI formation *via* the preferential decomposition of fluorinated anions, followed by the formation of poorly soluble inorganic salts, including MgF$_2$. The wider ESW for LiNFBS-0.35Mg(TFSI)$_2$-12H$_2$O than LiNFBS-12H$_2$O indicates that the addition of Mg(TFSI)$_2$ can result in the formation of a better-tolerated SEI consisting of less soluble MgF$_2$ than its Li counterpart.[10,11] This further suppresses the parasitic hydrogen evolution reaction (HER). As a result, in LiNFBS-0.35Mg(TFSI)$_2$-12H$_2$O, hierarchical interfacial protective layers consisting of a layer of hydrophobic NFBS$^-$ anions and a layer of the anion-derived scarcely-soluble Mg salt-based SEI demonstrated improved electrochemical oxidative and reductive stability.

To investigate the formation of a hierarchical passivation layer in the studied aqueous electrolytes, the SEI layer was formed on an Al current collector using potentiostatic polarization at −1.2 V for 20 h, and then the surface morphology was observed by SEM (Fig. 5(a)–(f)).[10,11] As shown in linear sweep voltammograms in the potential range from open circuit voltage (OCV) to −1.2 V (Fig. S5†), the reductive reaction was observed in all the electrolytes although the current density in LiNFBS-0.35Mg(TFSI)$_2$-12H$_2$O was significantly lower than that of other electrolytes, LiNFBS-12H$_2$O, LiTFSI-0.35Mg(TFSI)$_2$-12H$_2$O, LiNO$_3$-0.35Mg(TFSI)$_2$-12H$_2$O, and LiOTf-0.35Mg(TFSI)$_2$-12H$_2$O. The reductive current was attributed to the decomposition of water and anions, some of which contributed to the formation of an anion-derived passivation film on the Al substrate.
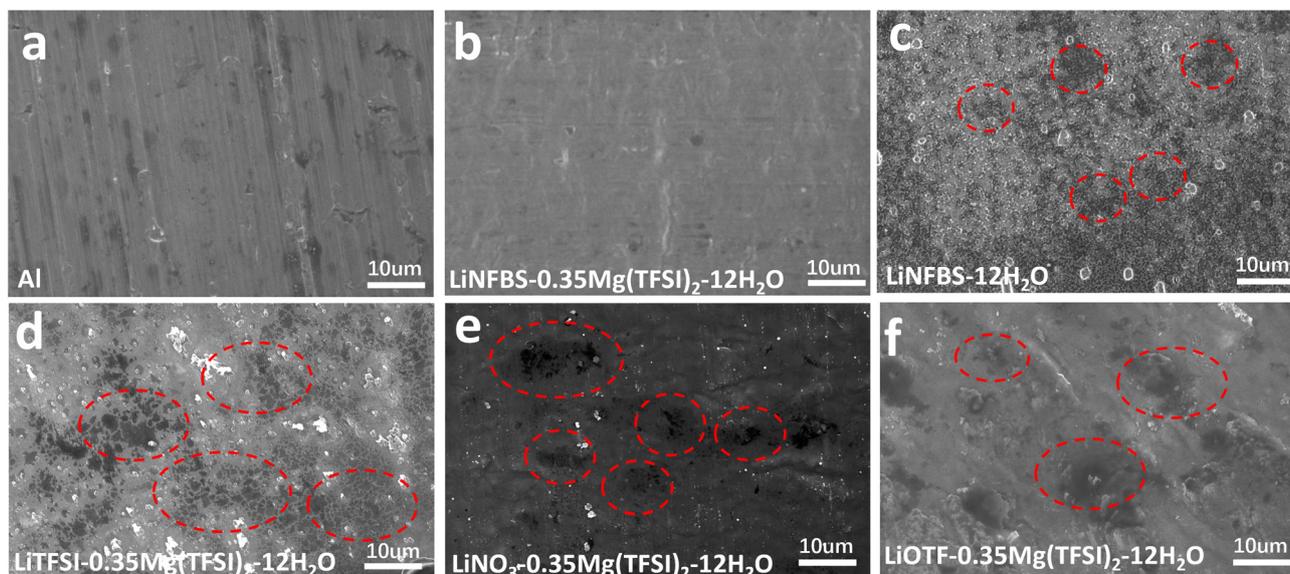

Fig. 5 SEM images of the Al electrode surface after potentiostatic polarization for 20 h at −1.2 V *vs.* Ag/AgCl using different electrolytes: (a) pristine Al foil; (b) LiNFBS-0.35 Mg(TFSI)$_2$-12H$_2$O; (c) LiNFBS-12H$_2$O; (d) LiTFSI-0.35Mg(TFSI)$_2$-12H$_2$O; (e) LiNO$_3$-0.35Mg(TFSI)$_2$-12H$_2$O; and (f) LiOTf-0.35Mg (TFSI)$_2$-12H$_2$O. The red dotted circular area represents an uneven passivation layer or a corroded Al foil electrode.

As shown in Fig. 5(a) and S6(a),† the original Al foil had a striped pattern with pits and microcracks caused by mechanical rolling because no additional materials were deposited on its surface. After the polarization at −1.2 V for 20 h, a highly dense and smooth film was formed on the surface of the Al electrode in LiNFBS-0.35Mg(TFSI)$_2$-12H$_2$O (Fig. 5(b) and S6(b)†). However, the Al electrode showed a surface morphology with numerous uneven indentations for LiNFBS-12H$_2$O in the absence of Mg(TFSI)$_2$ (Fig. 5(c) and S6(c)†). It appears that this surface film is not dense or stable enough to suppress the HER effectively. The gas evolution during the HER and Al corrosion in the basic environment were responsible for the degradation of the electrode surface (Fig. 5(c) and S6(c)†).[44] Similarly, as shown in Fig. 5(d)–(f), S6(d)–(f) and S7,† the surface morphology of the Al electrode was uneven for the electrolytes composed of the Li salts such as LiTFSI, LiNO$_3$ and LiOTf even with the same molar ratio of the Mg(TFSI)$_2$ additive.

The EIS data of the Al electrode were further obtained before and after potentiostatic polarization for 2 hours at −1.2 V $vs.$ Ag/AgCl using the studied electrolytes. Fig. S8(a)–(e)† shows Nyquist plots of the Al electrode cells using the electrolytes. The intermediate-frequency semicircle after polarization (except for the cell using LiTFSI-0.35Mg(TFSI)$_2$-12H$_2$O) can be ascribed to the anion-derived SEI formed on the Al electrode. For LiTFSI-0.35Mg(TFSI)$_2$-12H$_2$O, no semicircle was detected (Fig. S8(d)†), suggesting that the formation of the SEI film was incomplete. The SEI-based interfacial resistance, $R_{interface}$ (99 532 Ω) for LiNFBS-0.35Mg(TFSI)$_2$-12H$_2$O was significantly greater than those of LiNFBS-12H$_2$O (13 718 Ω), LiNFBS-0.35Mg(TFSI)$_2$ (49 380 Ω), and LiOTf-0.35Mg(TFSI)$_2$-12H$_2$O (47 532 Ω). The higher $R_{interface}$ value for

LiNFBS-0.35Mg(TFSI)$_2$-12H$_2$O suggests that a denser SEI film was formed via the synergetic effects of surface-active NFBS$^-$ and Mg salt additive on the surface of the Al electrode, leading to the improved ESW. Consequently, the SEM observation in Fig. 5 and EIS data (Fig. S8†) confirm that the interfacially localized, highly concentrated regions in LiNFBS-0.35Mg (TFSI)$_2$-12H$_2$O facilitated the formation of a dense and uniform SEI, thereby effectively preventing electrolyte decomposition.[45,46] However, LiNFBS-12H$_2$O, LiTFSI-0.35Mg (TFSI)$_2$-12H$_2$O, LiNO$_3$-0.35Mg(TFSI)$_2$-12H$_2$O, and LiOTf-0.35Mg (TFSI)$_2$-12H$_2$O are unable to form a robust passivation layer, leading to lower reductive stability.

Following cathodic polarization, X-ray photoelectron spectroscopy (XPS) measurements were performed on identical Al electrodes to further investigate the composition of the SEI films generated in various electrolytes. As shown in Fig. 6(a), the XPS spectrum of the Al electrode for Mg 2p in LiNFBS-0.35Mg(TFSI)$_2$-12H$_2$O is divided into four peaks at 52.8, 51.8, 50.6, and 49.4 eV, corresponding to the presence of MgCO$_3$, Mg(OH)$_2$ MgF$_2$, and MgO, respectively.[47–49] There was no LiF signal in the Li 1s spectrum, which is consistent with previous reports using the Mg[TFSI]$_2$ additive (Fig. S9(a)–(d)†).[10,11] The F 1s spectra at 685.3 eV, 687.6 eV, and 690.2 eV were identified as MgF$_2$, CF$_3$/CF$_x$, and CF$_2$–CF$_2$, respectively (Fig. 6(b)).[48,50–52] The O 1s spectral region involved five chemical components, O–C=O, C=O, C–O/Mg(OH)$_2$, MgCO$_3$ and MgO at 534.6, 533.7, 532.7, 531.45, and 529.7 eV, respectively (Fig. 6(c)).[49,53–57] For the C 1s spectrum, peaks at 289.2, 286.9, 286.0 and 284.8 eV corresponded to the characteristic peaks of MgCO$_3$, O–C=O/C=O, C–O, and C–C, respectively (Fig. 6(d)).[57,58] For the Al electrode after polarization in LiNFBS-12H$_2$O, Li 1s and F 1s spectra showed distinct peaks of
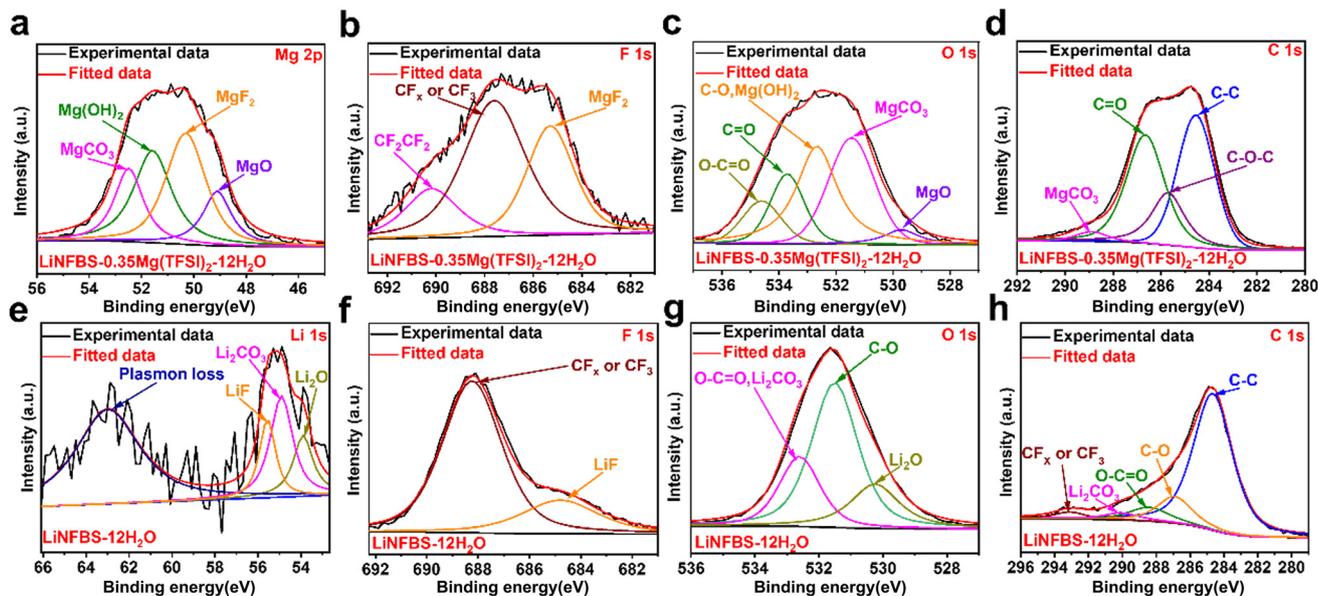

Fig. 6   XPS spectra of the Al electrode after polarization for 20 h at −1.2 V $vs.$ Ag/AgCl and LiNFBS-12H$_2$O: (a) Mg 2p, (b) F 1s, (c) O 1s, and (d) C 1s spectra in LiNFBS-0.35Mg(TFSI)$_2$-12H$_2$O and (e) Li 1s, (f) F 1s, (g) O 1s, and (h) C 1s in LiNFBS-12H$_2$O.

LiF at 55.6 and 684.8 eV, respectively (Fig. 6(e) and (f)). A peak at 688.4 eV was also observed in the F 1s spectrum and assigned to CF_x or CF_3 (Fig. 6(e)).[59] The peaks at 55.7 and 54.1 eV were assigned to Li_2CO_3 and Li_2O.[60,61] The O 1s (532.8 eV) and C 1s (290.2 eV) spectra also confirmed the presence of Li_2CO_3 (Fig. 6(g) and (h)).[62] Therefore, the poorly soluble Mg salt-based SEI is responsible for the enhanced ESW in LiNFBS-0.35Mg(TFSI)$_2$-12H$_2$O compared to that in LiNFBS-12H$_2$O without the Mg(TFSI)$_2$ additive.

The XPS analysis revealed that the SEI formed in LiNFBS-0.35Mg(TFSI)$_2$-12H$_2$O (Fig. 6(e)–(h)) was predominantly composed of the Mg salts and decomposition products

Table 2 Viscosity, ionic conductivity, molar concentration of Li salt and Mg salt, and density of the electrolytes, LiNFBS-0.35Mg(TFSI)$_2$-12H$_2$O, LiNO$_3$-0.35Mg(TFSI)$_2$-12H$_2$O, LiTFSI-0.35Mg(TFSI)$_2$-12H$_2$O, LiOTf-0.35Mg(TFSI)$_2$-12H$_2$O, and 1 M Li$_2$SO$_4$

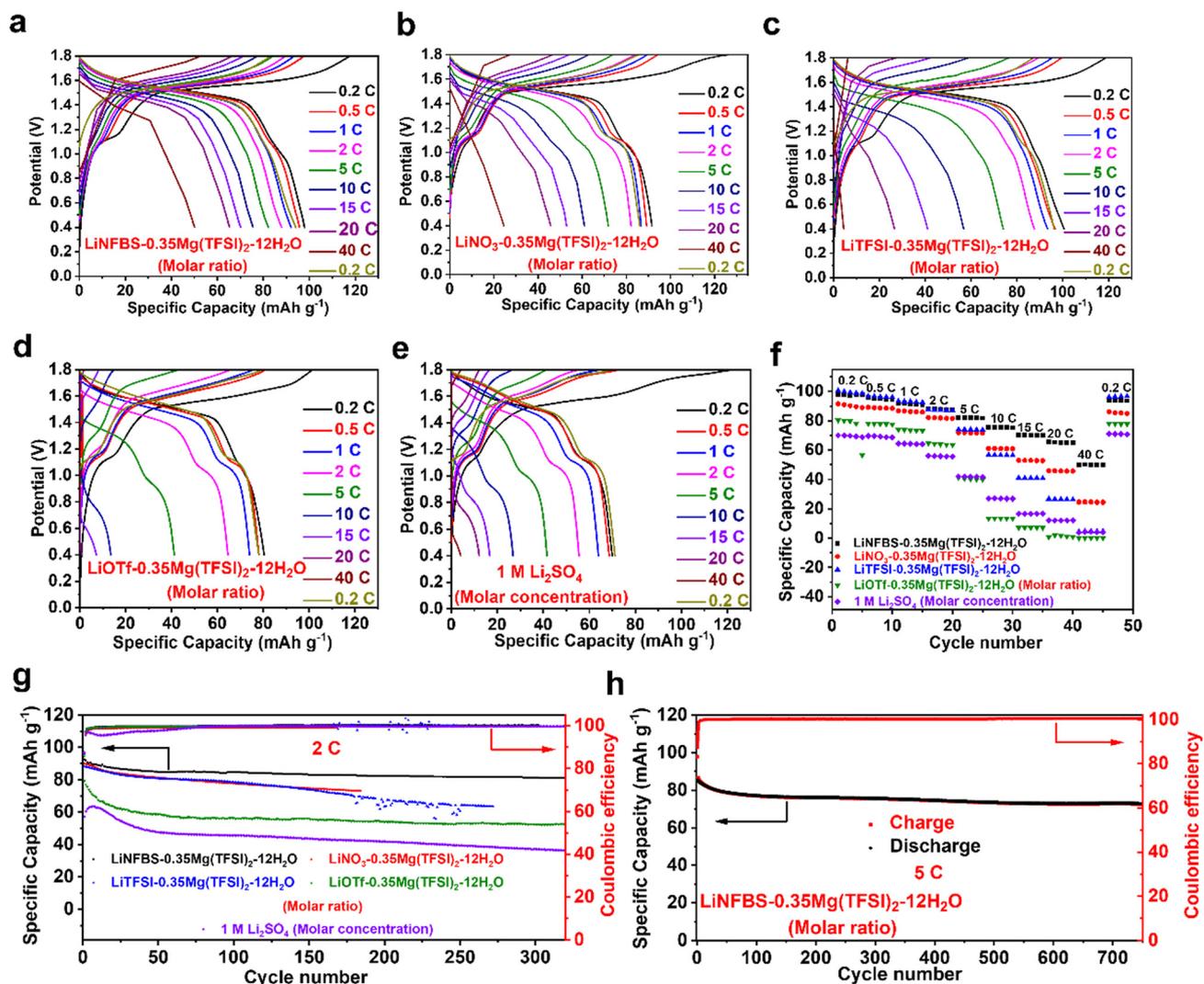| Electrolytes (molar ratio, 30 °C)	η (mPa s)	σ (mS cm^{-1})	Molar concentration (mol L^{-1})	ρ (g cm^{-3})
LiNFBS : 0.35Mg(TFSI)$_2$: 12H$_2$O	19.2	34.0	2.13 M : 0.74 M	1.54
LiNO$_3$: 0.35Mg(TFSI)$_2$: 12H$_2$O	3.7	79.4	2.84 M : 0.99 M	1.39
LiTFSI : 0.35Mg(TFSI)$_2$: 12H$_2$O	6.6	40.0	2.15 M : 0.76 M	1.53
LiOTf : 0.35Mg(TFSI)$_2$: 12H$_2$O	3.6	66.0	2.39 M : 0.84 M	1.38
Li$_2$SO$_4$: 54H$_2$O(1 M Li$_2$SO$_4$)	1.4	76.1	1 M	1.09

Fig. 7 (a)–(e) The charge–discharge curves, (f) rate performance at different current densities ranging from 0.2 to 40 C; (g) charge–discharge cycling performance of LTP/LMO full cells using electrolytes, LiNFBS-0.35Mg(TFSI)$_2$-12H$_2$O, LiNO$_3$-0.35Mg(TFSI)$_2$-12H$_2$O, LiTFSI-0.35Mg(TFSI)$_2$-12H$_2$O, LiOTf-0.35Mg(TFSI)$_2$-12H$_2$O, and 1 M Li$_2$SO$_4$ at a current density of 2 C; and (h) long cycling performance of the cell containing LiNFBS-0.35Mg(TFSI)$_2$-12H$_2$O at a current density of 5 C.

of the anions. We also detected similar XPS spectra assigned to the components of Mg salts for the SEI prepared in LiTFSI-0.35Mg(TFSI)$_2$-12H$_2$O, LiNO$_3$-0.35Mg(TFSI)$_2$-12H$_2$O, and LiOTf-0.35Mg(TFSI)$_2$-12H$_2$O (Fig. S10(a)–(l)†). However, the morphology of the SEI film is uneven, even with Mg(TFSI)$_2$ as shown in Fig. 5(d)–(f), leading to a narrower ESW in these electrolytes. These results corroborate that the interfacially localized, highly concentrated NFBS$^-$ anions play a significant role in the formation of a denser and smoother morphology of the SEI in LiNFBS-0.35Mg(TFSI)$_2$-12H$_2$O.

To demonstrate the advantages of the ILHCEs obtained with NFBS$^-$ in aqueous Li-ion batteries, galvanostatic charge–discharge measurements were performed using LTP/LMO full cells. In Table 2, the molar concentrations, density and ion transport properties of the studied electrolytes, LiNFBS-0.35Mg(TFSI)$_2$-12H$_2$O, LiTFSI-0.35Mg(TFSI)$_2$-12H$_2$O, LiOTf-0.35Mg(TFSI)$_2$-12H$_2$O, and LiNO$_3$-0.35Mg(TFSI)$_2$-12H$_2$O are summarized. All the electrolytes have similar molar concentrations of Li salt in the range of 2.13–2.83 M at equivalent molar ratios. LiNFBS-0.35Mg(TFSI)$_2$-12H$_2$O showed the highest viscosity (19.2 mPa s) and the lowest conductivity (34.0 mS cm^{-1}) among the studied electrolytes here.

Fig. 7(a)–(e) display charge–discharge curves of the LTP/LMO full cells at different current densities. The data for the cells using the reference electrolyte, (1 M Li$_2$SO$_4$) are also shown for comparison. The discharge capacities at different C rates are shown in Fig. 7(f). At a lower C rate of 0.2C, the cells using LiNFBS-0.35Mg(TFSI)$_2$-12H$_2$O and LiTFSI-0.35Mg(TFSI)$_2$-12H$_2$O delivered a higher discharge capacity of 100 mA h g^{-1}, whereas the discharge capacity decreased in the order of the anions of Li salts, OTf$^-$ < NO$_3^-$ < TFSI$^-$ ∼ NFBS$^-$. The lowest capacity was obtained for cells using the reference 1 M Li$_2$SO$_4$. The lower discharge capacity was attributed to more pronounced side reactions because of the narrower ESW. Despite the lower ionic conductivity of the electrolyte, the cell using LiNFBS-0.35Mg(TFSI)$_2$-12H$_2$O delivered higher capacity at higher C rates. Even at a current density of 40C, the LTP/LMO full cell still exhibited a discharge capacity exceeding 50 mA h

g^{-1} with more stable columbic efficiency (Fig. S11†). The cell potential of the discharge curves decreases more gently in this ILHCE, whereas it decreases steeply in other electrolytes. This is attributed to the improved mass transfer of Li ions in LiNFBS-0.35Mg(TFSI)$_2$-12H$_2$O with good wettability (Fig. 2) and a high Li$^+$ transference number (Fig. 3(c)), which effectively reduces the concentration overpotential within the cell.[63,64]

We also elucidated the charge–discharge cycling stability at current densities of 2 and 5 C (Fig. 7(g) and (h)). The LTP/LMO full cells using LiNFBS-0.35Mg(TFSI)$_2$-12H$_2$O retained a specific capacity of 81 mA h g^{-1} and an average columbic efficiency of 99.94% at a current density of 2 C even after 320 cycles. This capacity retention was much higher than those using LiNO$_3$-0.35Mg(TFSI)$_2$-12H$_2$O, LiTFSI-0.35Mg(TFSI)$_2$-12H$_2$O, LiOTf-0.35 Mg(TFSI)$_2$-12H$_2$O, and 1 M Li$_2$SO$_4$. Even after 750 cycles at a high current density of 5 C, the cell using the ILHCE still retained a specific capacity of 73 mA h g^{-1} and an average columbic efficiency of 100% (Fig. 7(g) and (h)). Compared to other ultra-high concentration and co-solvent electrolyte systems, LiNFBS-0.35Mg(TFSI)$_2$-12H$_2$O also demonstrates better rate performance and cycling stability (Table S4†).[65–67] The long-term cycling stability and high capacity retention can be attributed to the formation of a stable, dense, and smooth SEI at the interface. The better rate performance was ascribed to the improved mass transfer of Li ions as highlighted by t_{Li^+}^{NMR}. Additionally, as shown in Fig. S12 and S13,† LTP/LMO full cells using LiNFBS-0.35Mg(TFSI)$_2$-12H$_2$O exhibited stable charge–discharge curves without a significant increase in the overpotential during long-term cycling at rates of 2 and 5 C. This is a striking difference from the cell using other electrolytes, which showed a gradual increase in the overpotential with charge–discharge cycling. The stability of LiNFBS-0.35Mg(TFSI)$_2$-12H$_2$O in LTP/LMO full cells was also examined at a lower C-rate (Fig. S14†). The full cell delivered a discharge capacity of 96 mA h g^{-1} with a stable coulombic efficiency of 99.5% after 20 cycles at a current density of 0.2 C. The more stable charge–discharge behavior in
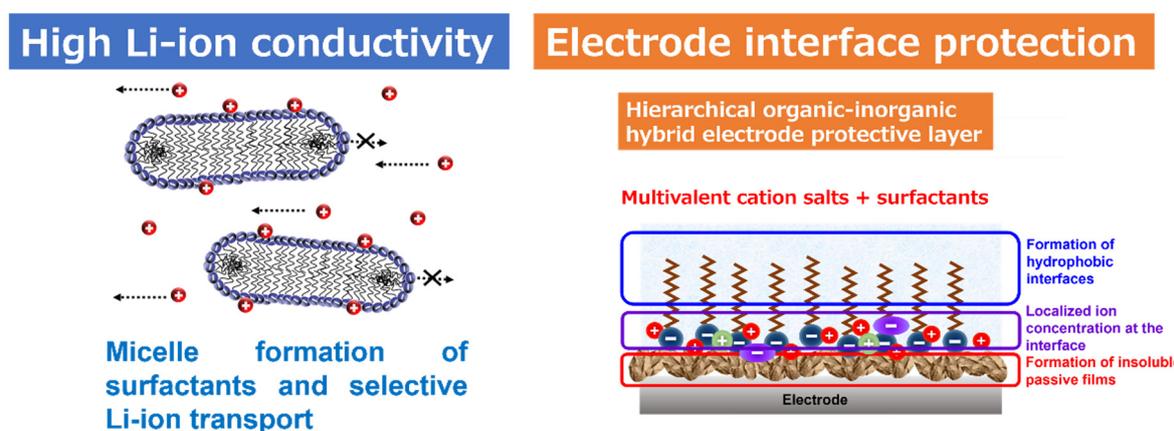
Scheme 1 Schematic illustration of the interfacially-localized high-concentration electrolytes: function in bulk solution and at the interface.

LiNFBS-0.35Mg(TFSI)$_2$-12H$_2$O is ascribed to the interfacially localized, highly concentrated assembly of NFBS$^-$ anions that reduce interfacial water and facilitate the formation of a denser and more uniform SEI consisting of poorly soluble Mg salts, further mitigating capacity degradation.

We aimed to develop environmentally friendly, low cost, and high-performance aqueous batteries through a rational design strategy that enhances the bulk and interfacial properties. The ILHCE concept demonstrated in this study is summarized in Scheme 1. Micellar aggregates of fluorinated surfactants were formed in the bulk solution through self-assembly of the surfactant monomers.[66,67] The considerable migration resistance of larger micellar aggregates in solution effectively limits anionic conduction, while allowing Li ions to be the major mobile species. This resulted in a high Li$^+$ transference number in the electrolyte. At the interface, surfactants were adsorbed and accumulated on the electrode. The long hydrophobic chains significantly reduced the amount of interfacial water, creating localized high-concentration regions in the Helmholtz plane.[17,18] The use of the divalent Mg(TFSI)$_2$ salt can efficiently suppress the decomposition of the electrolyte by forming insoluble passivation films such as MgF$_2$, MgCO$_3$, and MgO on the electrode surface.[10,11,50,51] The hierarchical surface-protection layer formed in ILHCEs eliminates the need for ultrahigh concentrated electrolytes, such as WiSE[5] or hydrate melt[4] to achieve a stable SEI while retaining the high Li-ion transport properties of aqueous electrolytes.

Conclusions

We proposed the concept of ILHCEs containing LiNFBS-0.35Mg(TFSI)$_2$-12H$_2$O. This surfactant was used in conjunction with divalent Mg salts to create a wide electrochemical stability window of 3.3 V. In comparison with WiSE and "hydrate melt" electrolytes, LiNFBS-0.35Mg(TFSI)$_2$-12H$_2$O exhibited a lower viscosity of 19.2 mPa s and a higher conductivity of 34.0 mS cm^{-1}. A comparative analysis of the electrochemical stability window, fundamental properties, SEI formation, and overall battery performance with different anions revealed that ILHCEs exhibited superior performance. In contrast to the other anions that either lack hydrophobic effects or exhibit lower hydrophobic effects, the greater hydrophobicity of NFBS$^-$ allows the creation of localized high-concentration ion regions at the interface, promoting the formation of a robust SEI. The restricted mobility of the micellar aggregates of NFBS$^-$ anions and the resulting high Li$^+$ transference number contributed significantly to the rate performance of LTP/LMO full cells. Even at a current density of 40 C, the cell using LiNFBS-0.35Mg(TFSI)$_2$-12H$_2$O exhibited a specific capacity of approximately 50 mA h g^{-1}. Owing to stable SEI formation, enhanced cycling stability was also achieved, with over 350 cycles at a current density of 2 C and over 750 cycles at a current density of 5 C. We believe that the concept of "interfacially-localized high-concentration electrolytes" will provide insight into rational electrolyte design for practical applications of aqueous lithium-ion batteries with high energy density, high rate performance, and excellent stability.

Data availability

Derived data supporting the findings of the following study are available from the corresponding author [K.U.] on request.

Conflicts of interest

There are no conflicts to declare.

Acknowledgements

References

1 C. Capello, U. Fischer and K. Hungerbühler, *Green Chem.*, 2007, **9**, 927–934.

2 Y. Yamada, K. Furukawa, K. Sodeyama, K. Kikuchi, M. Yaegashi, Y. Tateyama and A. Yamada, *J. Am. Chem. Soc.*, 2014, **136**, 5039–5046.

3 F. Philippi, M. Middendorf, K. Shigenobu, Y. Matsuyama, O. Palumbo, D. Pugh, T. Sudoh, K. Dokko, M. Watanabe, M. Schönhoff, W. Shinoda and K. Ueno, *Chem. Sci.*, 2024, **15**, 7342–7358.

4 Y. Yamada, K. Usui, K. Sodeyama, S. Ko, Y. Tateyama and A. Yamada, *Nat. Energy*, 2016, **1**, 16129.

5 L. Suo, O. Borodin, T. Gao, M. Olguin, J. Ho, X. Fan, C. Luo, C. Wang and K. Xu, *Science*, 2015, **350**, 938–943.

6 T. D. Pham, A. B. Faheem and K.-K. Lee, *Small*, 2021, **17**, 2103375.

7 K. Dokko, D. Watanabe, Y. Ugata, M. L. Thomas, S. Tsuzuki, W. Shinoda, K. Hashimoto, K. Ueno, Y. Umebayashi and M. Watanabe, *J. Phys. Chem. B*, 2018, **122**, 10736–10745.

8 Y. Ugata, M. L. Thomas, T. Mandai, K. Ueno, K. Dokko and M. Watanabe, *Phys. Chem. Chem. Phys.*, 2019, **21**, 9759–9768.

9 K. Xu, *Chem. Rev.*, 2004, **104**, 4303–4418.

10 S. Kondou, E. Nozaki, S. Terada, M. L. Thomas, K. Ueno, Y. Umebayashi, K. Dokko and M. Watanabe, *J. Phys. Chem. C*, 2018, **122**, 20167–20175.

11 S. Kondou, Y. Watanabe, K. Dokko, M. Watanabe and K. Ueno, *ChemElectroChem*, 2022, **9**, e202200061.

12 K. Dokko, N. Tachikawa, K. Yamauchi, M. Tsuchiya, A. Yamazaki, E. Takashima, J.-W. Park, K. Ueno, S. Seki,

N. Serizawa and M. Watanabe, *J. Electrochem. Soc.*, 2013, **160**, A1304.

13 S. Saito, H. Watanabe, K. Ueno, T. Mandai, S. Seki, S. Tsuzuki, Y. Kameda, K. Dokko, M. Watanabe and Y. Umebayashi, *J. Phys. Chem. B*, 2016, **120**, 3378–3387.

14 S. Chen, J. Zheng, D. Mei, K. S. Han, M. H. Engelhard, W. Zhao, W. Xu, J. Liu and J.-G. Zhang, *Adv. Mater.*, 2018, **30**, 1706102.

15 J. Zheng, S. Chen, W. Zhao, J. Song, M. H. Engelhard and J.-G. Zhang, *ACS Energy Lett.*, 2018, **3**, 315–321.

16 G. Kume, M. Gallotti and G. Nunes, *J. Surfactants Deterg.*, 2008, **11**, 1–11.

17 C. Wang, Y. Tan, Z. Jiang, X. Lin and S. Hu, *Colloid Polym. Sci.*, 2015, **293**, 3479–3486.

18 J. Eastoe, J. Dalton, P. Rogueda, D. Sharpe, J. Dong and J. R. P. Webster, *Langmuir*, 1996, **12**, 2706–2711.

19 S. Kondou, A. Morinaga, K. Hashimoto, Y. Katayama, K. Dokko, M. Watanabe and K. Ueno, *ChemElectroChem*, 2022, **9**, e202200870.

20 Y. Wang, F. Zhang, J.-A. Chen, X. Zhang, J. Wen, C. Wang and G. Huang, *J. Alloys Compd.*, 2023, **939**, 168704.

21 F. Junker, K. Michalski, G. Guthausen and M. Bunzel, *Carbohydr. Polym.*, 2021, **267**, 118232.

22 S. Roy, B. Biswas, N. Ghosh, P. C. Singh and J. A. Mondal, *J. Phys. Chem. C*, 2019, **123**, 27012–27019.

23 K. Ueno, K. Yoshida, M. Tsuchiya, N. Tachikawa, K. Dokko and M. Watanabe, *J. Phys. Chem. B*, 2012, **116**, 11323–11331.

24 A. Bernheim-Groswasser, R. Zana and Y. Talmon, *J. Phys. Chem. B*, 2000, **104**, 4005–4009.

25 S. P. Moulik, *Curr. Sci.*, 1996, **71**, 368–376.

26 M. J. Rosen and J. T. Kunjappu, *Surfactants and Interfacial Phenomena*, 2012, pp. 123–201, DOI: **10.1002/9781118228920.ch3**.

27 S. F. Burlatsky, V. V. Atrazhev, D. V. Dmitriev, V. I. Sultanov, E. N. Timokhina, E. A. Ugolkova, S. Tulyani and A. Vincitore, *J. Colloid Interface Sci.*, 2013, **393**, 151–160.

28 S. Pal, B. Bagchi and S. Balasubramanian, *J. Phys. Chem. B*, 2005, **109**, 12879–12890.

29 L. R. Fisher and D. G. Oakenfull, *Chem. Soc. Rev.*, 1977, **6**, 25–42.

30 C. Eypert-Blaison, L. J. Michot, B. Humbert, M. Pelletier and F. Villiéras, *J. Phys. Chem. B*, 2002, **106**, 730–742.

31 V. Starov, N. Ivanova and R. G. Rubio, *Adv. Colloid Interface Sci.*, 2010, **161**, 153–162.

32 K. M. Diederichsen, E. J. McShane and B. D. McCloskey, *ACS Energy Lett.*, 2017, **2**, 2563–2575.

33 H. K. Bergstrom, K. D. Fong, D. M. Halat, C. A. Karouta, H. C. Celik, J. A. Reimer and B. D. McCloskey, *Chem. Sci.*, 2023, **14**, 6546–6557.

34 Z. Yu, T. R. Juran, X. Liu, K. S. Han, H. Wang, K. T. Mueller, L. Ma, K. Xu, T. Li, L. A. Curtiss and L. Cheng, *Energy Environ. Mater.*, 2022, **5**, 295–304.

35 Y. Watanabe, Y. Ugata, K. Ueno, M. Watanabe and K. Dokko, *Phys. Chem. Chem. Phys.*, 2023, **25**, 3092–3099.

36 G. A. Giffin, A. Moretti, S. Jeong and S. Passerini, *J. Power Sources*, 2017, **342**, 335–341.

37 M. Schmeisser, P. Illner, R. Puchta, A. Zahl and R. van Eldik, *Chem. – Eur. J.*, 2012, **18**, 10969–10982.

38 H. Rupprecht and T. Gu, *Colloid Polym. Sci.*, 1991, **269**, 506–522.

39 L. K. Koopal, E. M. Lee and M. R. Böhmer, *J. Colloid Interface Sci.*, 1995, **170**, 85–97.

40 R. Zhang and P. Somasundaran, *Adv. Colloid Interface Sci.*, 2006, **123–126**, 213–229.

41 M. Grossutti, J. J. Leitch, R. Seenath, M. Karaskiewicz and J. Lipkowski, *Langmuir*, 2015, **31**, 4411–4418.

42 W. Sun, L. Tang, W. Ge, Y. Fan, X. Sheng, L. Dong, W. Zhang, H. Jiang and C. Li, *Adv. Sci.*, 2024, **11**, 2405474.

43 A. K. Pennathur, C. Tseng, N. Salazar and J. M. Dawlaty, *J. Am. Chem. Soc.*, 2023, **145**, 2421–2429.

44 E. B. Carneiro-Neto, M. C. Lopes and E. C. Pereira, *J. Electroanal. Chem.*, 2016, **765**, 92–99.

45 Z. Huang, J. Ren, W. Zhang, M. Xie, Y. Li, D. Sun, Y. Shen and Y. Huang, *Adv. Mater.*, 2018, **30**, 1803270.

46 W. Liu, P. Liu and D. Mitlin, *Adv. Energy Mater.*, 2020, **10**, 2002297.

47 X. Q. Tran, S. D. McDonald, Q. Gu, S. Matsumura and K. Nogita, *J. Mater. Res.*, 2016, **31**, 1316–1327.

48 M. Matsui, H. Kuwata, D. Mori, N. Imanishi and M. Mizuhata, *Front. Chem.*, 2019, **7**, 7.

49 M. R. A. Cruz, E. Luévano-Hipólito, R. Garza-Hernández and L. M. Torres-Martínez, *J. Mater. Sci.*, 2022, **57**, 18739–18753.

50 Z. Zhao, B. Nian, Y. Lei, L. Zhao, M. N. Hedhili, D. Guo, Z. Shi, W. Zhao, J. K. El-Demellawi, Y. Wang, Y. Zhu, K. Xu and H. N. Alshareef, *Adv. Mater.*, 2024, 2402626.

51 C. Peng, L. Xue, Z. Zhao, L. Guo, C. Zhang, A. Wang, J. Mao, S. Dou and Z. Guo, *Angew. Chem., Int. Ed.*, 2024, **63**, e202313264.

52 A. N. Mansour, D. G. Kwabi, R. A. Quinlan, Y.-C. Lu and Y. Shao-Horn, *J. Electrochem. Soc.*, 2016, **163**, A2911.

53 Z. Sun, Y. Tan, Y. Zhan, K. Li, W. Dou, C. Wang, X. Lin, R. Yuan, J. Yan, M. Zheng and Q. Dong, *Small Methods*, 2023, **7**, 2201289.

54 X. Shen, H. Zhang, X. Li, P. Li, Y. Zhao, Y. Wang and J. Wang, *Regener. Biomater.*, 2022, **9**, rbac068.

55 Y. Bourlier, M. Bouttemy, O. Patard, P. Gamarra, S. Piotrowicz, J. Vigneron, R. Aubry, S. Delage and A. Etcheberry, *ECS J. Solid State Sci. Technol.*, 2018, **7**, P329.

56 D. Dong, Y. Zhang, Y. Xiao, T. Wang, J. Wang and W. Gao, *J. Power Sources*, 2021, **503**, 230049.

57 A. S. May and E. J. Biddinger, *Green Chem.*, 2023, **25**, 8687–8697.

58 G. Li, H. Wang, X. Shi, C. Yang, R. Wang, B. He, J. Jin, Y. Gong, A. Tang and H. Yang, *Chem. Commun.*, 2022, **58**, 11276–11279.

59 X.-D. Lin, Y. Gu, X.-R. Shen, W.-W. Wang, Y.-H. Hong, Q.-H. Wu, Z.-Y. Zhou, D.-Y. Wu, J.-K. Chang, M.-S. Zheng, B.-W. Mao and Q.-F. Dong, *Energy Environ. Sci.*, 2021, **14**, 1439–1448.

60 S. Jo, B. Kwon, J. Oh, J. Lee, K. Park and K. T. Lee, *J. Mater. Chem. A*, 2022, **10**, 5520–5529.

61 K. N. Wood and G. Teeter, *ACS Appl. Energy Mater.*, 2018, **1**, 4493–4504.

62 G. Jiang, J. Liu, J. He, H. Wang, S. Qi, J. Huang, D. Wu and J. Ma, *Adv. Funct. Mater.*, 2023, **33**, 2214422.

63 L. Que and W. Chen, *J. Power Sources*, 2023, **557**, 232536.

64 C. Heubner, U. Langklotz, M. Schneider and A. Michaelis, *J. Electroanal. Chem.*, 2015, **759**, 91–94.

65 D.-Y. Lan, X.-F. Qu, Y.-T. Tang, L.-Y. Liu and J. Liu, *J. Electrochem.*, 2022, **28**, 6.

66 Z. Ma, J. Chen, J. Vatamanu, O. Borodin, D. Bedrov, X. Zhou, W. Zhang, W. Li, K. Xu and L. Xing, *Energy Storage Mater.*, 2022, **45**, 903–910.

67 Y. Wang, T. Ou, Y. Dong, L. Chen, Y. Huang, D. Sun, W. Qiang, X. Pei, Y. Li and Y. Tan, *Adv. Mater.*, 2024, **36**, 2311009.